BioCapt® Single-Use

Aktiver Luftkeimsammler

Testfertiger, aktiver Ersatz für Sedimentationsplatten

- Kontinuierliche Luftprobenahme und Überwachung
- Testfertiger Ersatz für Sedimentationsplatten
- Weniger Handhabungsschritte und weniger falsch-positive Untersuchungen
- Für den mobilen oder remote Einsatz
- Auswahl verschiedener Agarformulierungen und Flussraten
- Erfüllt ISO 14698-1 und den erwarteten EU-GMP-Annex 1 Einweg-Anforderungen
- Verwendung mit aktiven Luftkeimsammler-Instrumenten für eine vollständig validierte Lösung

Mehr erfahren

PARTICLE MEASURING SYSTEMS®
a spectris company

Kontaktieren Sie uns für mehr Informationen:
www.pmeasuring.de
T: +49 351 8896 3850
E: pmsgermany@pmeasuring.com

ARTICLE

BIOTECHNOLOGY BIOENGINEERING WILEY

Synchrotron radiation-based microcomputed tomography for three-dimensional growth analysis of *Aspergillus niger* pellets

Henri Müller[1] | Charlotte Deffur[1] | Stefan Schmideder[1] | Lars Barthel[2] |
Tiaan Friedrich[1] | Lukas Mirlach[1] | Jörg U. Hammel[3] | Vera Meyer[2] |
Heiko Briesen[1]

[1]School of Life Sciences Weihenstephan, Chair of Process Systems Engineering, Technical University of Munich, Freising, Germany

[2]Chair of Applied and Molecular Microbiology, Institute of Biotechnology, Technische Universität Berlin, Berlin, Germany

[3]Helmholtz-Zentrum hereon, Institute of Materials Physics, Geesthacht, Germany

Correspondence
Heiko Briesen, Chair of Process Systems Engineering, Technical University of Munich, Gregor-Mendel-Str. 4, 85354 Freising, Germany.
Email: heiko.briesen@tum.de

Abstract

Filamentous fungi produce a wide range of relevant biotechnological compounds. The close relationship between fungal morphology and productivity has led to a variety of analytical methods to quantify their macromorphology. Nevertheless, only a μ-computed tomography (μ-CT) based method allows a detailed analysis of the 3D micromorphology of fungal pellets. However, the low sample throughput of a laboratory μ-CT limits the tracking of the micromorphological evolution of a statistically representative number of submerged cultivated fungal pellets over time. To meet this challenge, we applied synchrotron radiation-based X-ray microtomography at the Deutsches Elektronen-Synchrotron [German Electron Synchrotron Research Center], resulting in 19,940 3D analyzed individual fungal pellets that were obtained from 26 sampling points during a 48 h *Aspergillus niger* submerged batch cultivation. For each of the pellets, we were able to determine micromorphological properties such as number and density of spores, tips, branching points, and hyphae. The computed data allowed us to monitor the growth of submerged cultivated fungal pellets in highly resolved 3D for the first time. The generated morphological database from synchrotron measurements can be used to understand, describe, and model the growth of filamentous fungal cultivations.

KEYWORDS
3D image analysis, *Aspergillus niger*, computed tomography, filamentous fungi, morphology, pellet growth

1 | INTRODUCTION

Filamentous fungi are an indispensable part of industrial biotechnology. During submerged cultivation in bioreactors with a volume of several hundred cubic meters, these cell factories produce chemicals, enzymes, organic acids, antibiotics, and other drugs (Cairns et al., 2018; Füting et al., 2021; Meyer et al., 2020; Ward, 2012; Wösten, 2019).

The morphology of filamentous fungi is closely linked to the productivity (Cairns, Zheng, et al., 2019; Lyu et al., 2023; Tegelaar et al., 2020; Veiter et al., 2018). Their macromorphologies, which they adopt during submerged cultivation, range from non-aggregated

hyphae called dispersed mycelia to loosely aggregated clumps of hyphae, to densely packed spherical hyphal networks called pellets (Papagianni, 2004; Veiter et al., 2018). Titer, vitality, and hydrophobicity of the spore inoculum, cultivation conditions, and the genetic background all influence the morphology that finally develops (Papagianni, 2004; Wucherpfennig et al., 2010; Zhang & Zhang, 2016). The bioprocess can be positively and negatively influenced by the developed (Ehgartner et al., 2017). Dispersed mycelia grow rapidly, but cause a non-Newtonian behavior and a high viscosity of the cultivation broth, which in turn lowers the oxygen transfer rate. On the other hand, cultivations with pellets mostly show a Newtonian fluid behavior with low viscosity, but the dense hyphal structures limit nutrient and oxygen supply to inner parts of the pellet, reducing growth and growth-associated product formation (Cairns, Zheng, et al., 2019; Hille et al., 2009; Veiter et al., 2020; Wittier et al., 1986).

Since filamentous morphology is a key parameter for the effectiveness of fungal bioprocesses, a thorough understanding of the growth of the hyphal structures and the development of the morphology is crucial. Hyphal networks of fungal pellets are large and complex. Furthermore, their inner 3D structures, for example, the spatial distribution of hyphal material and tips, affect their productivity. Therefore, classical light microscopy is insufficient to study the complete and inner pellet morphology in 3D. The only method that can resolve the complete non-destructed 3D structure of a fungal pellet bases on μ-computed tomography (μ-CT) of freeze-dried pellets and subsequent 3D image analysis to locally detect the amount of hyphal material, tips, and branching points—the micromorphology of a pellet (Schmieder, Barthel, Friedrich, et al., 2019). However, a small field of view and long measurement times at the required high local resolution massively reduce the sample throughput. On the contrary, high heterogeneities between fungal pellets during cultivation make it necessary to measure the morphology of a few hundred pellets in each cultivation time step to be statistically representative.

Up to now, μ-CT measurements of hundreds of pellets for multiple cultivation times cannot be efficiently achieved with lab-scale computer tomography. We have overcome this limitation in this study by harnessing μ-CT based on synchrotron X-ray radiation at the Deutsches Elektronen-Synchrotron–DESY (Hamburg, Germany). The high photon flux and large field of view of synchrotron radiation enables the generation of 3D images of up to 579 pellets in less than 10 min. Furthermore, we updated our previously developed image acquisition and analysis methods (Schmieder, Barthel, Friedrich, et al., 2019) by the development of a standardized sample holder, the automatic segmentation of pellets, the detection of spores within pellets—the spore core of a pellet, and the automatic analysis of micromorphological properties in a single programming language (MATLAB, version 2020b). Since 2D image analysis tools of microscopic images enable a high sample throughput and are the state of the art for following the macromorphological development of fungal pellets, for example, size and shape of filamentous fungi (Cairns, Feurstein, et al., 2019;

Müller et al., 2022; Posch et al., 2012; Willemse et al., 2018), we compared 2D data of the same *Aspergillus niger* cultivations in Müller et al. (2022) with the data generated from the synchrotron measurements.

Based on μ-CT measurements and growth simulations, we previously presented a universal law to correlate the 3D structure and diffusive mass transport of oxygen and nutrients through hyphal networks (Schmieder, Barthel, Muller, et al., 2019; Schmieder et al., 2020). In combination with statistically representative 3D data from synchrotron measurements, it is now possible to model the growth and substrate availability during filamentous fungal cultivations. Complementing modeling, this pure 3D growth data will lead to a holistic understanding of the morphological evolution of fungal pellets.

2 | MATERIALS AND METHODS

2.1 | Cultivation, sampling, and preparation of pellets

In this study, we analyzed samples from the same cultivations of the hyperbranching *A. niger* Δ*racA* strain MF22.4 (Fiedler et al., 2018; Kwon et al., 2013), which were already used for our development of a 2D high-throughput image analysis pipeline (Müller et al., 2022). Thereby, two 5 L Erlenmeyer flasks with 1 L complete medium, based on a minimal medium described in Meyer et al. (2010) supplemented with 1% (w/v) yeast extract and 0.5% (w/v) casamino acids, were inoculated with $2.5 \cdot 10^6$ spores/mL. For a detailed description of the inoculum preparation, we refer to Müller et al. (2022). The replicated cultivations (flask A and B) were performed for 48 h at 30°C with a rotational speed of 90 RPM in an Infors HT Multitron Standard shaker (Infors AG).

For μ-CT measurements, pellet samples were taken after 9 h, 9.5 h, and every hour from 10 h until 32 h. The last sample was taken after 48 h of cultivation, resulting in a total number of 26 sampling times. At every sampling time, 1 mL of culture volume with *A. niger* pellets was carefully pipetted into a 1.5 mL reaction tube (Sarstedt AG & Co. KG) using a 10 mL serological pipette (Sarstedt AG & Co. KG). To generate freeze dried fungal pellet samples, we followed our previously developed protocol (Schmieder, Barthel, Friedrich, et al., 2019). Thereby, the culture sample was washed three times with sterile deionized water and deep frozen in liquid nitrogen while pellets were floating in water. Subsequently, the samples were freeze dried, resulting in one reaction tube with multiple freeze dried pellets per sampling time. Within the study of Schmieder, Barthel, Friedrich, et al. (2019), we showed that freeze-drying preserves fungal morphology. For synchrotron radiation-based microcomputed tomography (SR-μ-CT) measurements, the freeze-dried fungal pellets were carefully transferred into sample holders (Figure 1a) for each sampling time. These newly developed and standardized sample holders consist of a polyether ether ketone (PEEK) base, a hollow Kapton® tube with inside diameter of 3.2 mm, and a PEEK cap.
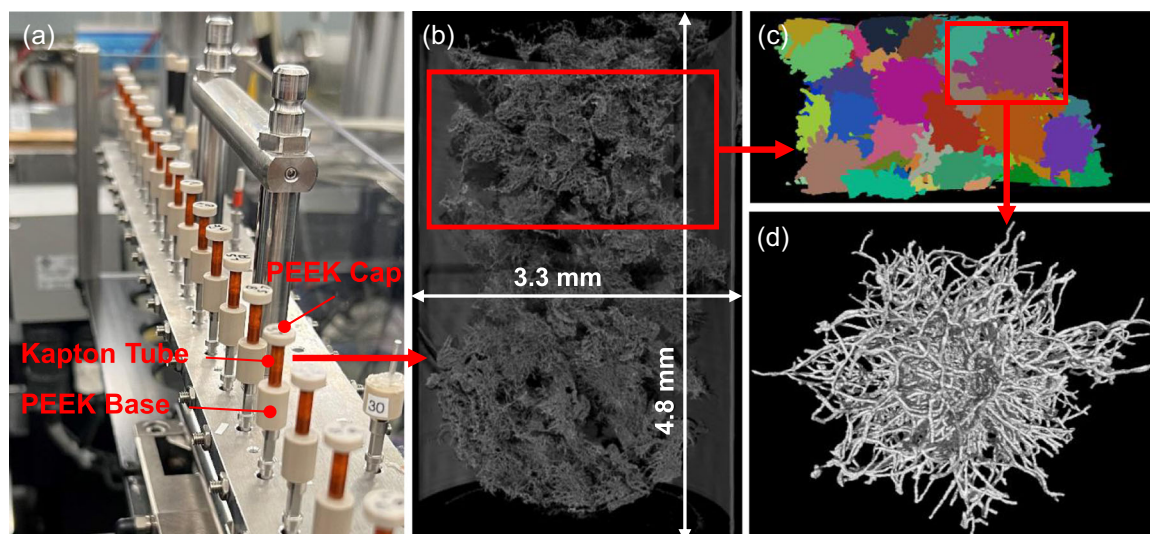
FIGURE 1 Sample preparation, microtomography, and image processing. (a) Sample holders with freeze dried pellets from different cultivation times at the microtomography beamline P05. (b) Synchrotron radiation based X-ray microtomography with a voxel size of 1.28 µm. (c) By the marker-controlled watershed segmentation labeled pellets. (d) Segmented and binarized pellet with an equivalent diameter of 557 µm.

Kapton® and PEEK provide high X-ray transparency and resistance (Antimonov et al., 2015; Kurtz, 2012).

2.2 | Synchrotron µ-CT

SR-µ-CT of *A. niger* pellets was achieved with the Imaging Beamline P05 (Greving et al., 2014; Haibel et al., 2010; Wilde et al., 2016) operated by the Helmholtz-Zentrum hereon at the PETRA III storage ring (Deutsches Elektronen-Synchrotron—DESY). For each measurement, the sample holder containing the pellets of the corresponding sampling time was placed on a sample pin that fits in the sample rotation stage. The rotation axis of the sample holder was adjusted once to the center of the field of view and adopted for all further measurements. Imaging was performed with a photon energy of 18 keV with 30 ms exposure time per projection. For each tomographic scan, 2401 projections equally spaced between 0° and 180° were recorded using a 20 MP CMOS camera system with an effective pixel size of 0.64 µm and a field of view of 3.32 × 2.46 mm (Lytaev et al., 2014). The sample detector distance was set to 100 mm. We performed two scans for each sample to increase the field of view in vertical direction. The volumes were reconstructed with twofold binning based on the filtered back projection algorithm, which was implemented in a custom reconstruction pipeline (Moosmann et al., 2014) based on MATLAB (MathWorks) and the Astra Toolbox (Van Aarle et al., 2015, 2016; Palenstijn et al., 2011). The reconstructed bottom and upper volumes of a sample were stitched together with an overlap of 120 slices by a custom stitching algorithm based on MATLAB. The resulting sample volume has a size of 2595 × 2595 × 3718 voxels with a binned voxel size of 1.28 µm (Figure 1b). The 3D images were saved as image stacks with floating point numbers resulting in a size of 93.3 GB for each image. Since we

measured 26 sampling times for each cultivation flask, we generated 4.85 TB of 3D image data for analysis.

2.3 | Image processing

Our developed image processing pipeline was completely established in MATLAB (Version 2020b) and can be divided into three parts: (1) The automatic segmentation into individual pellets from the total sample volume consisting of multiple pellets (Figure 1b–d). (2) The detection of spores within each pellet, which define the center of a pellet. (3) The local detection of tips, branching points, and hyphal material for each pellet.

Part (3) is based on the previously developed image analysis methods described in Schmieder, Barthel, Friedrich, et al. (2019). To unify and automate image processing, some of the code was reprogrammed into MATLAB, which is now the only platform used for the analysis. This allowed the automatic processing of 19,940 pellet objects at once. The newly developed image processing steps are described in more detail below.

2.3.1 | Pellet segmentation

The total sample volume with multiple pellets was divided into two equal size subvolumes along the rotation axis to reduce computational effort. The slices of a subvolume were converted to a 16-bit gray level image. The gray level image represents pellets, parts of the sample holder and air. The sample holder base was removed by determining the gray value gradient in vertical z-direction between the transition of the PEEK base and air. Slices before the gradient depicting the PEEK base were deleted. The remaining gray level

image including pellets, and the sample holder Kapton® tube was binarized by setting a gray value threshold, which was calculated with Otsu's method (Otsu, 1979). Subsequently, the binarized tube was removed based on a normalized cross-correlation (Haralick & Shapiro, 1992; Lewis, 1995). Thereby, the position and tilt of a cylindrical template that corresponded to the internal volume of the Kapton® tube was calculated. By masking the binarized subvolume with the cylindrical template, a binary image depicting only pellets as foreground objects was obtained. To label and segment the pellets into individual ones, a marker-controlled watershed segmentation (Meyer, 1994) was performed. For this method, closed pellet spheres were generated by dilating the pellets with a spherical structured element and filling remaining holes in the dilated pellets (Schmideder et al., 2020). Subsequently, a distance transformation was performed on the complemented binary image with closed pellet spheres, resulting in a distance image with the Euclidean distances of each voxel of closed pellet spheres to the closest background voxel. To calculate separate markers representing the inner part of each closed pellet sphere, voxels that had a Euclidean distance greater than 18 voxels from the background on the resulting distance image were binarized into foreground markers. For each marker, a complete pellet sphere was labeled by the watershed segmentation (Figure 1c). By masking all voxels on the original gray level subvolume with zero except a corresponding labeled pellet sphere, a gray level image was obtained representing only a single pellet. The resulting 16-bit gray level images representing only one single pellet were cropped according to pellet size (Schmideder et al., 2020). Other than the deletion of the sample holder base, the same segmentation procedure was repeated for the second subvolume. The PEEK cap was not in the field of view of the second SR-μ-CT scan.

2.3.2 | Detection of spores

The gray level images of single pellets were directly used for the detection of spores in the center of pellets. Spores appear as bright spherical shells with low gray values in their centers. To enhance the isolated low gray values inside of spores, bottom-hat filtering (MATLAB function "imbothat") was performed using a spherical structured element with a diameter of 5 voxels. The radius choice of the structuring element aimed to completely cover the low gray values inside of the potential spores. The gray values of the resulting bottom-hat filtered image, in which the formerly low gray values in the center of spores are now bright gray values, were scaled to the interval [0–1] and binarized with a fixed threshold of 0.3. This guaranteed that only high gray values that represented potential spore objects were binarized into the foreground. Since potential spores are only detected based on the low gray values inside of the bright spherical shells of spores, large objects with a volume of at least 30 voxels were deleted. Afterwards, clustering of the remaining spore objects was performed as another control mechanism for spore detection. Thereby, the centroid of each spore object was calculated and clustered with the dbscan algorithm (Ester et al., 1996). The

number of neighboring spore centroids was set to 10 within a search radius of 15 μm. Since spores are densely agglomerated within pellets, the choice of cluster parameters was based on a relatively small radius and high minimum number of neighbors. Identified clusters with the highest number of spores and those with at least 100 spores were finally recognized together as spore agglomerate within the pellet—the spore core of the pellet. The yellow dots within pellets in Figure 2, middle row, mark the centroids of the detected spores. Afterwards, the mass center of the clustered spore centroids (Figure 2, bottom row, red dot) and the volume of the spore core based on the convex hull (MATLAB function "convhull") was calculated. The obtained center of mass of the spore core defined the pellet center (Figure 2, bottom row, red dot).

2.3.3 | Determination of local hyphal fractions, tips, and branching point densities

To differentiate between the hyphae of a pellet and the background, the cropped gray level images were binarized by setting a gray value threshold that was calculated using Otsu's method (Otsu, 1979). After binarization, connected objects smaller than $5000 \, \mu m^3$ were deleted to eliminate small impurities among the hyphae. Figure 2, top row, shows segmented and binarized pellets after 16, 24, and 32 h. The local detection of tips and branching points based on the skeleton of the binarized 3D pellet image is described by Schmideder, Barthel, Friedrich, et al. (2019).

The hyphal fraction is defined as the ratio between the volume of hyphae within a representatively sized pellet section and the total volume of the pellet section (Schmideder, Barthel, Muller, et al., 2019). A similar definition applies to the number density of tips and branching points, that is, the number of tips or branching points divided by the representative total volume. To characterize the number densities of tips, branching points and the hyphal fractions of a pellet radially along its distance from the pellet center, these micromorphological features were analyzed in shells of the pellet (Figure 2, bottom row left). The width of shells was set to 15 μm and the inner sphere had a radius of 50 μm. The geometric center of the shells is defined by the center of mass of the spore core. Since the spore core can be embedded eccentrically in the pellet, the shells were constrained by the convex hull of the pellet. Otherwise, for example, the hyphal fractions along the distance from the pellet center would be strongly underestimated if the spore core is located at the outer edge of a pellet. To compute the constrained volume of the shell, the intersection between the convex hull and the corresponding shell was calculated (Jacobson & Panozzo, 2018) as shown in Figure 2, bottom row right. To avoid that the hyphal fraction is determined in intersections that have a very small volume, the minimum intersection volume was set to at least 10% of the corresponding total spherical shell. Finally, the hyphal fraction for each shell was calculated by the ratio between the hyphal volume within an intersection and the total volume of the intersection. The number density of tips and branching points along the distance from the pellet center was calculated accordingly.
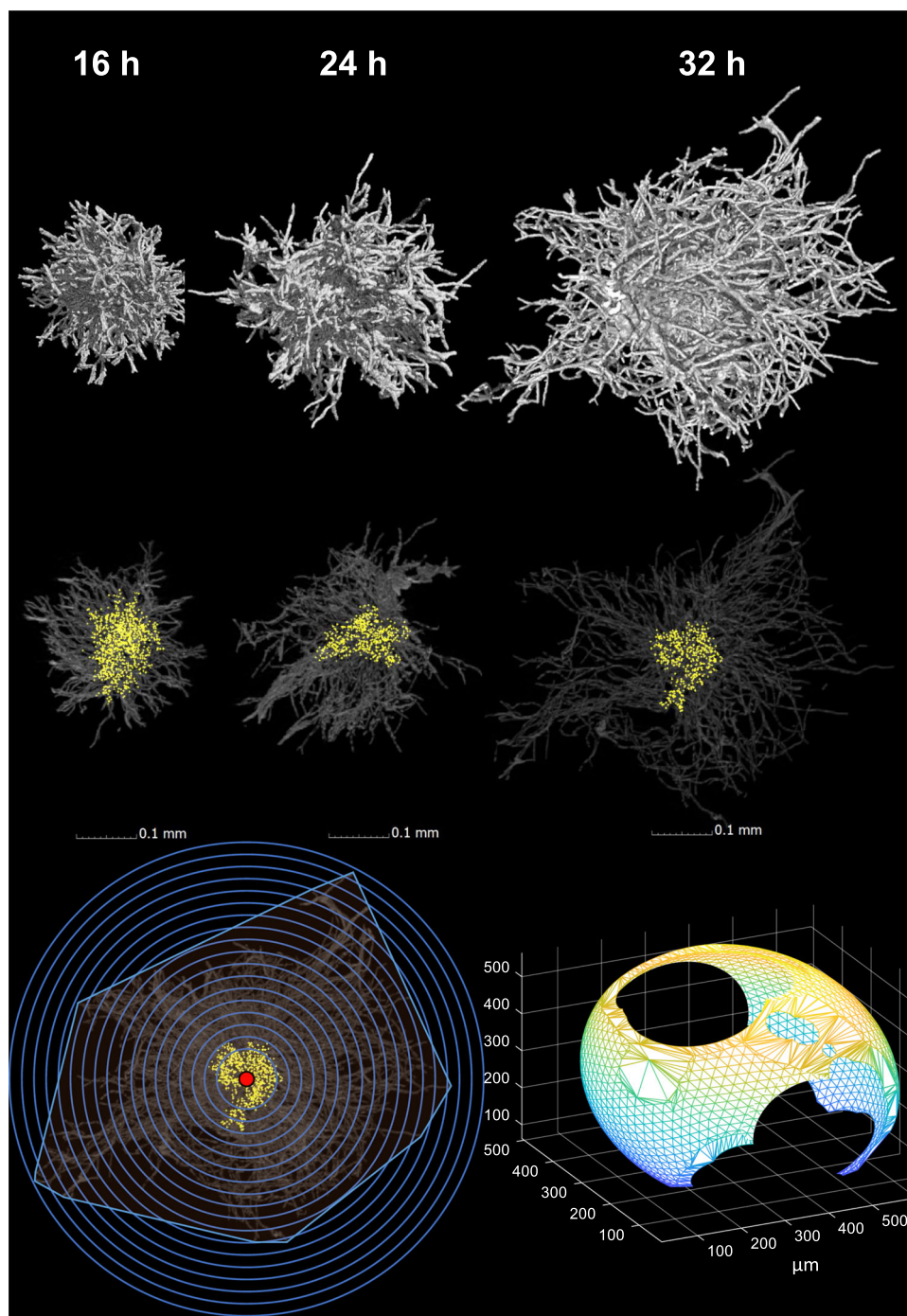
FIGURE 2 Segmented *Aspergillus niger* pellets from different sampling times and detected spores defining the growth center of a pellet. Top row: Segmented and binarized *A. niger* pellets from 3D image processing based on SR-μ-CT after 16, 24, and 32 h of cultivation. The pellets shown were clustered as regular pellets. Middle row: Detected spore centroids (yellow dots) based on bottom-hat filtering of the 16-bit gray level pellet images. Bottom row left: Spherical shells (blue) centered on the growth center (red dot) of the pellet. The growth center is calculated as the mass center of the detected spore centroids (yellow dots). The outer spherical shells form intersections with the convex hull of the pellet (light blue). Bottom row right: Calculated 3D intersection between the convex hull and a corresponding spherical shell. The hyphal fraction, tip, and branching point densities as a function of the distance from the growth center are analyzed in the spherical shells or intersections. SR-μ-CT, synchrotron radiation-based microcomputed tomography.

2.3.4 | Determination of global morphology features

Global morphology features are those that are calculated based on the complete pellet structure. The volume equivalent spherical diameter of a pellet and the spore core were calculated using the volume of the convex hull of the pellet and the spore core, respectively, as $d = \sqrt[3]{\frac{6 \cdot V_{ConvHull}}{\pi}}$. The total number of tips, branching points, and spores for each pellet were determined by summing up the corresponding segmented objects for each pellet. Furthermore, the total volume of hyphae for each pellet V_{Hyphae} was calculated by counting all foreground voxels of the binarized pellet and multiplying it with the volume per voxel (Schmieder, Barthel, Friedrich, et al., 2019).

To calculate the average diameter of the hyphae d_{Hyphae} for each pellet, we performed an Euclidean distance transformation (MATLAB function "bwdist") (Maurer et al., 2003) of the complemented binarized pellet image. In addition, we computed the skeleton (MATLAB function "bwskel") (Kerschnitzki et al., 2013; Lee et al., 1994) of the binarized pellet image. By masking all voxels of the distance image with zero except for those representing the skeleton of the pellet, we obtained the regional radii of hyphae. Based on the regional hyphal radii, we calculated the arithmetic mean of the hyphal diameter d_{Hyphae}. Using the total volume of hyphae V_{Hyphae} and the average diameter of hyphae d_{Hyphae}, the total hyphal length L_{Hyphae} for each pellet was calculated as $L_{Hyphae} = \frac{4 \cdot V_{Hyphae}}{\pi \cdot d_{Hyphae}^2}$.

The average branch length of pellets, which is the average length between two branching points or a branching point and a tip, was estimated as $\frac{L_{Hyphae}}{\text{Total number of tips} + \text{Total number of branching points}}$. Furthermore, the hyphal growth unit (HGU) of pellets was calculated by $\frac{L_{Hyphae}}{\text{Total number of tips}}$ as originally defined by Caldwell and Trinci (1973). A video illustrating important image processing steps can be found on YouTube. The video was created using μ-CT scans of *Rhizopus stolonifer* pellets performed with a lab-scale μ-CT system.

2.4 | Data processing

2.4.1 | Preprocessing of pellet data by Gaussian mixture modeling (GMM) clustering

Various artifacts can occur during sample preparation for SR-μ-CT measurements and segmentation of the pellets during image processing. Components in the medium can adhere to freeze dried pellets or be entrapped between the sampled pellets. Furthermore, pellet samples may become entangled during freeze drying and cannot be properly separated by image analysis. In addition, breakage can occur during the transfer to the sample holder. During image processing, pellets can be cropped when dividing the total sample volume into two subvolumes. Therefore, different control mechanisms were established to filter potential pellet objects into artifacts and regular pellets.

First of all, potential pellet objects with volume equivalent spherical diameters smaller than 100 μm and larger than 1000 μm

were considered to be artifacts and were not considered for further data analysis. This can be justified by the 2D image analysis of the cultivations (Müller et al., 2022), where no pellets outside of this size range could be identified after 9–48 h of cultivation. Furthermore, pellet objects with no detected spore cores were disregarded, since they were considered impurities or dispersed mycelia. In addition to these hard cut-off parameters, a soft clustering was performed using GMM (Bishop, 2009) with two classes, artifacts and regular pellets. Therefore, three morphological features for each pellet resulting from 19,940 segmented pellet objects from flask A and B were used for model creation. The three features are visualized in a sketch in Supporting Information: Figure S1a: (1) the calculated hyphal fraction within the inner sphere with a radius of 50 μm centered around the center of mass of the spore core. For example, entangled pellets have a lower hyphal fraction in their inner sphere (Supporting Information: Figure S1b). (2) The volume ratio between the convex hull of a pellet object and the volume of the circumscribed sphere of a pellet object centered on the center of mass of the spore core. For example, damaged and cropped pellets have an eccentricity where the spore core is not centered in the pellet, resulting in a smaller volume ratio compared to whole pellets (Supporting Information: Figure S1c,d). (3) The axis ratio of the shortest and longest major axis of a pellet object. For example, pellets cropped due to image processing obtain a smaller axis ratio (Supporting Information: Figure S1d).

Since all features had a seemingly log-normal distribution, they were logarithmized to obtain a more stable clustering result. Furthermore, the features were standardized (MATLAB function "zscore") to have a mean of zero and standard deviation of one. For the sake of stability, 10 replicates of the model were built with the one with the highest log likelihood as the final model. Finally, all pellets of the corresponding features were classified against the chosen model by calculating the largest posterior probability (Bishop, 2009).

Only potential pellet objects classified as regular pellets were used for the determination of growth parameters and 3D growth analysis.

2.4.2 | Determination of growth parameters

For fitting the growth parameters with the experimental 3D image data and biomass, we used the exponential growth phase of the culture, which was identified to be after 9–22 h in Müller et al. (2022).

The exponential growth of biomass (X) and hyphal volume of pellets (V) was formulated as $X = X_0 \cdot e^{\mu_X \cdot t}$ and $V = V_0 \cdot e^{\mu_V \cdot t}$, respectively. The initial value of the biomass X_0 and the hyphal volume V_0 in the exponential equations were estimated as unknown variables at the same time with the growth parameters μ_X and μ_V. Based on a model proposed from Schuhmann and Bergter (1976), which was later used by Buschulte (1992) to describe the exponential growth in the early cultivation phase, we obtained the mean apical growth

—WILEY—⏋ 7

velocity α in µm per hour per tip and branching rate β in number of tips per µm per hour from the experimental image analysis data. Thus, we fitted α and β by simultaneously solving the proposed ordinary differential equations $\frac{dL}{dt} = \alpha \cdot N(t)$ and $\frac{dN}{dt} = \beta \cdot L(t)$. Here, $N(t)$ is the total number of tips and $L(t)$ is the total hyphal length of a pellet depending on time t. The MATLAB solver ODE45 was used for integration of the simple system of first order differential equations. The parameter estimation was done by minimizing the sum of square errors of X, V separately, and N and L combined over the recorded times using the iterative trust-region method (MATLAB function "lsqnonlin"). The 95% confidence intervals (CI) were computed using a nonlinear least squares method (MATLAB function "nlparci") and the Jacobian matrix on the found solution.

3 | RESULTS AND DISCUSSION

In this study, we demonstrate the potential of SR-µ-CT measurements and subsequent 3D image analysis to investigate the morphological development of filamentous pellets. As a first case study, a replicated submerged cultivation (flask A and B) of *A. niger* MF22.4 was investigated in detail. This strain is characterized by the deletion of the Rho GTPase RacA, causing an approximately 30% increase in branching without altering the growth rate in submerged cultivation. Furthermore, its potential use as a platform strain for enhanced glucoamylase production was demonstrated, making it promising for industrial applications (Fiedler et al., 2018; Kwon et al., 2013). Table 1 summarizes the number of pellets for each cultivation time originating from flask A and B, which were finally clustered as regular pellets and used for 3D growth analysis. Regular pellets have a volume equivalent spherical diameter between 100 and 1000 µm and own a spore core (Material and Methods Section 2.4.1). In addition, due to soft GMM clustering, regular pellets obtain a calculated hyphal fraction near the center of mass of the spore core (Feature 1) in the range of 0.12–0.35, a volume ratio between the convex hull and the volume of the circumscribed sphere

(Feature 2) in the range of 0.25–0.59, and an axis ratio in the range of 0.39–0.93 (Feature 3).

Since fungal parameters describing 3D pellet growth are rarely found in literature for method evaluation, the section starts with a comparison between 2D and 3D image analysis of the identical cultivation. Afterwards, global and local morphology parameters for each cultivation time will be presented. The section closes with a critical evaluation of the developed methodology.

3.1 | Comparison between results of 2D and 3D image analysis and spore detection

Figure 3 shows a direct comparison of the calculated mean area/volume equivalent circular/spherical diameters of pellets and spore cores from cultivation flask A and B over time using 2D and 3D image data, respectively. The 2D data were replicated here from Müller et al. (2022).

After 9 h, the calculated 2D and 3D mean area/volume equivalent circular/spherical diameter is 230 and 195 µm, respectively. Until 12 h, the volume-based (3D) mean equivalent diameters and their standard deviations are below the area-based (2D) data. These differences may be caused by the nonspherical shape of young pellets resembling the shape of their fractured spore cores. Based on the 3D volume data, we calculated a mean axis ratio between the minor and major axes per pellet of 0.58 after 9 h which increased to 0.64 after 13 h (Supporting Information: Figure S3). When measuring equivalent diameters of nonspherical objects with their projections, which is the case when calculating an area-based circular equivalent diameter, a difference is usually found between area- and volume-based equivalent diameters. After 32 h, a higher 3D mean equivalent diameter of 513 µm can be observed compared to 450 µm (2D). Here, the 2D image analysis is unable to detect individual protruding hyphae from pellets that are more common after later cultivation times, possibly due to substrate limitations. For example, denser pellets with short and highly branched hyphae are formed under higher dissolved oxygen tensions (Cui et al., 1998; Wongwicharn

TABLE 1 Analyzed number of pellets for each flask and cultivation time.

Time (h)	9	9.5	10	11	12	13	14	15	16	17	18	19	20
Flask A	52	63	80	96	491	208	579	237	278	437	525	546	241
Flask B	64	163	128	29	202	140	206	3	387	298	464	299	383
Total	116	226	208	125	693	348	785	240	665	735	989	845	624
Time (h)	21	22	23	24	25	26	27	28	29	30	31	32	48
Flask A	420	292	265	180	208	223	96	65	151	127	128	107	77
Flask B	355	219	255	154	166	222	233	140	128	112	66	101	68
Total	775	511	520	334	374	445	329	205	279	239	194	208	145

Note: The numbers indicate the number of SR-µ-CT analyzed pellets clustered as regular pellets by the applied Gaussian mixture model.

Abbreviation: SR-µ-CT, synchrotron radiation-based microcomputed tomography.
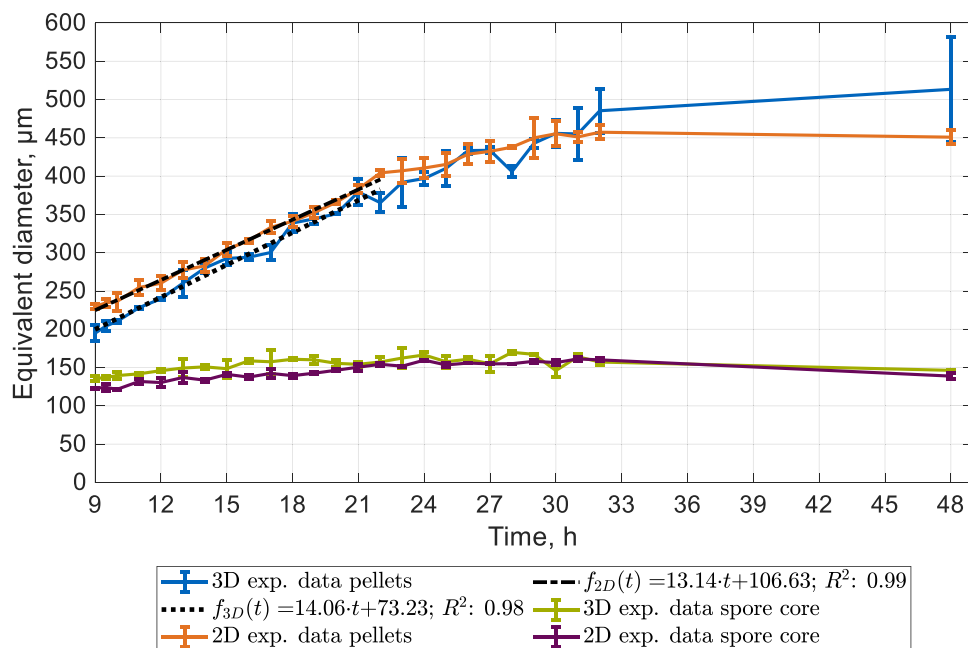
FIGURE 3 Comparison of the calculated mean equivalent diameters of pellets and spore cores as a function of cultivation time using 2D and 3D image data. The 2D data were taken from Müller et al. (2022). The graphs for 3D data were calculated with the data obtained by the 3D image analysis of the SR-μ-CT images. The shown data of equivalent diameters are mean values, calculated with the mean of flasks A and B. Spore cores are detected spore agglomerates within pellets. The error bars indicate the standard deviation between the mean of flasks A and B. The functions $f_{3D}(t)$ and $f_{2D}(t)$ were calculated by linear regression models. The slope of the calculated functions (14.06 μm h^{-1} 3D and 13.14 μm h^{-1} 2D) indicate the growth velocity of the pellet equivalent diameter after 9–22 h. SR-μ-CT, synchrotron radiation-based microcomputed tomography.

et al., 1999). Accordingly, we calculated a higher HGU and average branch length starting after 21 h (see following Section). Furthermore, the convex hull used to calculate the 3D volume-based equivalent diameter is placed around the outermost tips of a pellet resulting in a higher equivalent diameter in contrast to the 2D image analysis. The standard deviations between the means of the replicated flasks A and B are in the range of the ones from the 2D image analysis and demonstrate high reproducibility of the sampling method for 3D imaging and the developed 3D image analysis pipeline. Higher standard deviations are observed after 31, 32, and 48 h, which may be due to an insufficient number of sampled pellets for the increasing heterogeneity of the cultivation after later sampling times (Müller et al., 2022). In addition to the small deviations of the mean equivalent diameters from 2D and 3D image data, a similar constant growth velocity of 13.14 μm h^{-1} (2D) and 14.06 μm h^{-1} (3D) of the pellet mean equivalent diameter was calculated with a simple linear regression model (Figure 3). Please note that in Müller et al. (2022), a constant growth velocity of 12.6 μm h^{-1} is reported, compared to the growth velocity of 13.14 μm h^{-1} used in this contribution. The reason for this is that for the assessment of the growth velocity reported in Müller et al. (2022), only the results from flask A have been used. Revisiting our previous results, we decided to use the data from both (flask A and B) for determination of an averaged growth velocity. Figure 3 also shows the mean equivalent diameter of the identified spore cores in the pellets for each cultivation time. The same trend and

similar values of the 2D and 3D data can also be observed here. After 9 h, a 3D volume-based mean equivalent diameter of 136 μm was calculated compared to 123 μm based on the 2D data. After 24 h, the mean equivalent diameters increased to 166 μm (3D) and 159 μm (2D). In Müller et al. (2022), we assumed that growth of hyphae within spore cores enlarges the spore cores, however, the number of detected spores for each pellet also increases (Figure 4). The boxplots in Figure 4 show the number of spores for each pellet for all analyzed pellets (flasks A and B) and the mean number of spores per pellet. After 9 h, a mean number of 767 spores and after 24 h, 1233 spores per pellet could be detected. This increase suggests that non-germinated spores within spore cores still swell, since more spores can be detected by the 3D image analysis due to their enlargement. Thus, the growth of hyphae not necessarily enlarges the spore core (Müller et al., 2022), but there is an ongoing swelling of non-germinated spores within the spore core. Non-germinated spores within pellets are also reported by El-Enshasy (2011) and Lyu et al. (2023). With the exception of the early and final cultivation times, a relatively constant number of spores per pellet was identified, for example, after 12–32 h, indicating high reproducibility of spore detection. In Müller et al. (2022), approximately 1265 spores per pellet were calculated, assuming that all spores had agglomerated and all spore agglomerates had built a pellet. In this study, we were able to identify a mean of 1038 spores per pellet, calculated with 11,157 analyzed regular pellets.
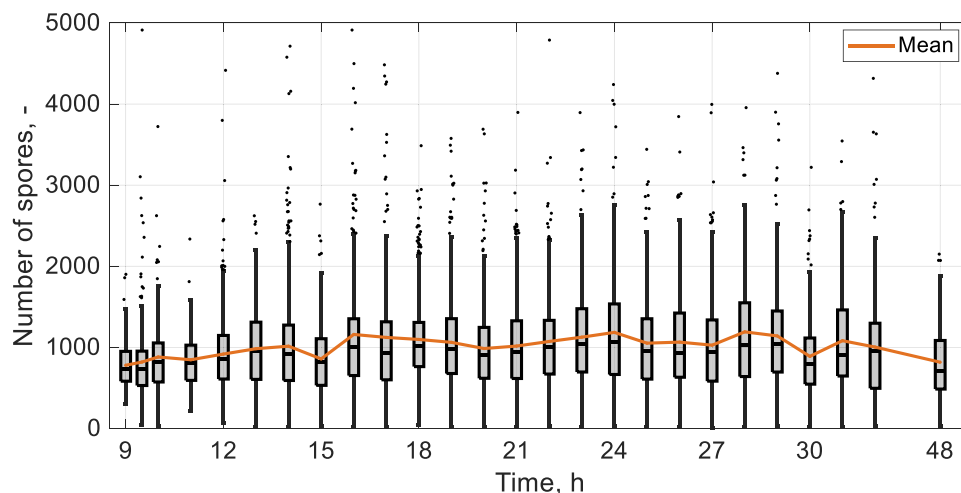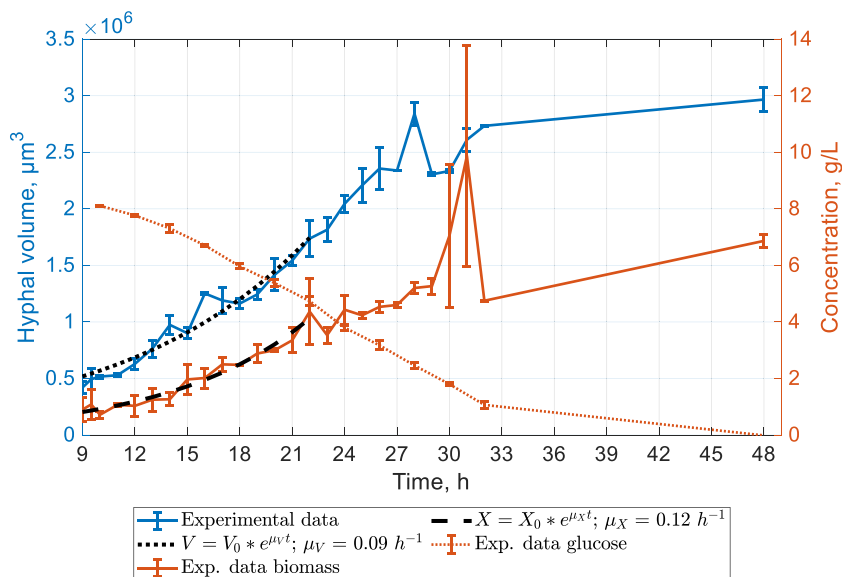
FIGURE 4 Boxplots representing the number of spores of pellets for each cultivation time for all analyzed pellets from flasks A and B. Black lines within the boxes mark the median. The outliers are indicated by scattered black dots. The whiskers and the outliers were calculated by 1.5 times the interquartile range. The orange graph shows the mean number of spores of pellets for each cultivation time. The data were determined by the 3D image analysis based on μCT images. μCT, microcomputed tomography.

FIGURE 5 Mean hyphal volume of pellets (left ordinate, blue) as well as biomass and glucose concentration (right ordinate, orange) as a function of cultivation time. The mean hyphal volumes of pellets were calculated with the mean hyphal volumes of flasks A and B. The error bars indicate the standard deviations between flasks A and B. The hyphal volumes were determined by 3D image analysis based on SR-μ-CT images. The orange gridlines and the right ordinate show the mean biomass (solid line) and glucose (dotted line) concentration in medium of flasks A and B. Biomass and glucose concentrations were experimentally determined and taken from Müller et al. ([2022](#)). The functions for biomass concentration $X(t)$ and hyphal volume of pellets $V(t)$ depending on time were used to fit the growth rate of biomass μ_X and hyphal volume of pellets μ_V. SR-μ-CT, synchrotron radiation-based microcomputed tomography.

After 32–48 h, a decrease of the mean equivalent diameter and the number of spores can be observed in Figures [3](#) and [4](#). The decreased mean number of spores per pellet from 974 after 32 h to 793 after 48 h supports the hypothesis in Müller et al. ([2022](#)) that pellets may break completely or partially at their spore core, supposedly because of glucose depletion in the medium (Figure [5](#)). Parts breaking out from the spore core of pellets were reported by Buffo et al. ([2020](#)).

3.2 | Global morphology development of pellets

Figure [5](#) provides an overview of the development of the mean hyphal volume of pellets from cultivation flasks A and B (left ordinate)

over time (abscissa). Furthermore, the mean biomass and glucose concentration from flasks A and B (right ordinate) is shown over time replicated from Müller et al. ([2022](#)). In contrast to the linear increase of the equivalent diameter (Figure [3](#)), the hyphal volume of the pellets and the biomass of the culture increases exponentially in the early growth phase when no substrate limitations occur (Wucherpfennig et al., [2010](#)). Based on the hyphal volume data from the 3D image analysis, we calculated a growth rate of pellets μ_V of 0.09 h^{-1} after 9–22 h within a 95% CI ranging from 0.08 h^{-1} to 0.11 h^{-1}. From the experimentally determined biomass (Müller et al., [2022](#)), a growth rate μ_X of 0.12 h^{-1} was calculated for the same cultivation period within a 95% CI ranging from 0.11 to 0.14 h^{-1}. It must be noted that the shown biomass data were determined with the dry weight of the complete culture including

dispersed mycelia (Müller et al., 2022). The hyphal volume in Figure 5 was calculated using pellets only. Therefore, we assume that the difference between the calculated growth rates is due to the growth of dispersed mycelia, which usually increases after early cultivation times with a higher growth rate compared to pellets (Kurt et al., 2018; Papagianni & Mattey, 2006; Veiter et al., 2018). After 32–48 h, a reduced increase of the biomass can be observed due to glucose limitation, which is in accordance with the analyzed hyphal volume from the 3D image analysis.

Figure 6a shows the mean total hyphal length of pellets from flasks A and B over time which increases from 35.36 to 169.12 mm after 9–32 h. Since the total hyphal length for each pellet is calculated based on the total hyphal volume and the average hyphal diameter for each pellet, it is slightly overestimated, since the spores within pellets are included in the hyphal volume for each pellet. However, the size of the spore core remains relatively constant over cultivation time and has almost no influence on the obtained apical growth velocity of hyphal tips. Based on the proposed model of Schuhmann and Bergter (1976), we calculated an apical growth velocity α per hyphal tip of 9.3 µm h^{-1} after 9–22 h within a 95% CI ranging from 7.9 to 10.6 µm h^{-1}. Since hyphae do not grow straight, but extend curved, we obtained a smaller increase of the mean equivalent radius per pellet (see the previous section), which is also assumed in modeling approaches of fungal pellets. For example, the change of the pellet radius is usually modeled as $r_{Pellet}(t) = \gamma \cdot \alpha \cdot \psi_{Tip} \cdot t + r_0$, where γ is a factor, taking into account that hyphae grow curved, and ψ_{Tip} is the growth activity, which describes the saturation kinetics related to the substrate supply (similar to Michaelis–Menten kinetics) (Buschulte, 1992; King, 1998). Using the increase of the mean equivalent radius, which was calculated to be 14.06 µm h^{-1}·0.5, we calculated γ as the ratio between the equivalent radius and the apical growth velocity, which is 0.76. Buschulte (1992)

FIGURE 6 Mean total hyphal length, number of tips, and branching points of pellets as a function of cultivation time, which were used to calculate the hyphal growth unit (HGU) and average branch length. (a) Mean total hyphal length of pellets as a function of cultivation time for flask A and B. The error bars indicate the standard deviations between flasks A and B. The total hyphal length was calculated based on the total hyphal volume V_{Hyphae} and the hyphal diameter d_{Hyphae} for each pellet as $L_{Hyphae} = \frac{4 \cdot V_{Hyphae}}{\pi \cdot d_{Hyphae}^2}$. The total hyphal volume and the hyphal diameter were determined by 3D image analysis based on SR-µ-CT images. The differential equation $\frac{dL}{dt}$ was used to fit the apical growth velocity of tips α. (b) Mean total number of tips (orange) and branching points (blue) of pellets as a function of cultivation time for flask A and B. The error bars indicate the standard deviations between flasks A and B. The differential equation $\frac{dN}{dt}$ depending on $L(t)$ was used to fit the branching rate β. The total number of tips and branching points for each pellet were determined by 3D image analysis based on SR-µ-CT images. (c) Mean (blue) and mean average branch length (orange) of pellets as a function of cultivation time for flasks A and B. The error bars indicate the standard deviations between flasks A and B. The HGU was calculated as $\frac{\text{Total hyphal length}}{\text{Total number of tips}}$ for each pellet. The average branch length was calculated as $\frac{\text{Total hyphal length}}{\text{Total number of tips + Total number of branching points}}$ for each pellet. SR-µ-CT, synchrotron radiation-based microcomputed tomography.

estimated a value of 0.8 for *Streptomyces tendae* within his modeling approach. The comparison between the growth velocity of the equivalent pellet radius derived from 2D image analysis and the apical growth velocity of the tips based on 3D image analysis indicates that these values were calculated in a correct range.

The calculated average diameters of hyphae per pellet, which also influence the calculated total hyphal length, are in accordance with manually measured hyphal diameters. After, 9, 24, and 48 h, the average hyphal diameters and standard deviations from the 3D image analysis of all analyzed pellets (flasks A and B) were calculated at 3.9 ± 0.22, 4.6 ± 0.49, and $4.4 \pm 0.56\,\mu m$, respectively. The standard deviations indicate the differences between the analyzed pellets. 100 manually measured hyphal diameters of pellets were determined in differential interference contrast images (DIC) for selected cultivation times resulting in mean values of 4.4 ± 0.46, 4.4 ± 0.52, and 4.0 ± 0.53 after 9, 24, and 48 h, respectively. The DIC images were generated in Müller et al. (2022). Furthermore, Colin et al. (2013) measured hyphal diameters of *A. niger* ranging from 2.5 to 4.5 μm, depending on cultivation conditions, indicating that our calculated hyphal diameters from the 3D image analysis are within a sufficiently precise range.

Figure 6b shows the mean number of tips and branching points of pellets from cultivation flasks A and B over time. After 9–18 h, the number of tips and branching points increased from 400 to 853 and from 202 to 672, respectively. Contrary to the branching points, the tips show higher variations in the mean values and between flasks A and B, expressed by the standard deviations. Since tips move and do not remain stable in pellets compared to branching points, they are detected mainly in the outermost parts of the pellet, where different factors can influence the tip detection by 3D image analysis. For example, tips can touch other hyphae resulting in the detection of a branching point instead of a tip. Furthermore, remaining freeze-dried impurities from the medium can cause hyphae to stick together, making tip detection less technically reproducible. However, the course of the tips and branching points shows a similar behavior until 21 h. After 22 h, the number of branching points overrates the number of tips pointing toward hyphal anastomosis, a well described phenomenon occurring in filamentous fungi including species of the genus *Aspergillus*. Hyphae not only grow by hyphal extension and branching but can also fuse with other hyphae in the older part of the mycelium, thus forming an interconnected mycelium that can distribute nutrients much more easily (Glass, 2004). Based on the model of Schuhmann and Bergter (1976) and the detected tips, we calculated a branching rate β of $0.00042\,\mu m^{-1}\,h^{-1}$ within a 95% CI ranging from 0.00029 to $0.00054\,\mu m^{-1}\,h^{-1}$.

Figure 6c shows the mean HGU and the mean average branch length, which is the average length between two branching points or a branching point and a tip. The HGU, originally defined by Caldwell and Trinci (1973), expresses the mean hyphal length available per tip of a pellet. Experiments for young mycelium have shown that the HGU remains constant if the number of tips/branching points and consequently the total hyphal length increases exponentially (Dynesen & Nielsen, 2003; Trinci, 1974). If the HGU becomes

constant for a growing mycelium, the average branch length is also constant. In Figure 6c, contrary to the HGU, the mean average branch length remains almost constant at around 63 μm until 21 h and subsequently increases to about 86 μm after 32 h. Since the average branch length takes both parameters into account, the number of tips and branching points taken into account softens the effect of possibly underestimated tips by means of the image analysis. Furthermore, during the constant exponential growth phase of a pellet, the average branch length can be easily interpreted as the length between two branching points or a branching point and a tip. We therefore recommend introducing the average branch length as a parameter to characterize the growth of fungal pellets by means of 3D image analysis. In the literature, an HGU of 108 μm for young mycelium of *A. niger* can be found, which corresponds to our analyzed values after 14 and 18 h (Colin et al., 2013).

3.3 | Local morphology development of pellets

To our knowledge, this study is the first to measure an incomparable high number of fungal pellets three-dimensionally over several cultivation time steps. Therefore, especially the data in Figure 7a,c cannot be verified with data from the literature.

Figure 7a,c show the mean hyphal fraction, branching point, and tip density of pellets from cultivation flasks A and B over the distance from the pellet center, which is defined as the center of mass of the spore core. The small standard deviations indicate a high reproducibility of the developed method inclusive of the sampling of the cultivation flasks, the transfer into the sample holder for 3D imaging, and the developed image analysis. In Figure 7a, the hyphal fraction in the outer pellet regions increases with time. Since the spore core defines the pellet center and has an equivalent diameter of about 146 μm after 12 h (Figure 3), the hyphal fraction up to 50 μm from the pellet center represents mainly the solid fraction of the spore core, ranging from 20.5% after 18 h to 22% after 32 h, and is also the densest part of a pellet. After 48 h, it can be observed that the hyphal fraction within inner pellet regions decreased compared to after 24 and 32 h. Since the detected mean number of spores per pellet also decreased after 32–48 h from about 1000 to 800, we are assuming that parts from the spore core are breaking out from the pellet and lead to a reduced hyphal fraction. However, the hyphal fractions after 48 h show the highest standard deviations, possibly pointing at autophagic processes reported for later stages of *A. niger* batch cultivations, which are associated with cell death (Nitsche et al., 2013). Various biological effects including breakage of pellets or lysis effects due to changes in carbon source or limitation can lead to a higher population heterogeneity (Tegelaar et al., 2020), which was observed in Müller et al. (2022) after 48 h under glucose limitation (Figure 5). Figure 7b,c indicate the branching point and tip density. Contrary to tips, branching points do not move during pellet growth. This can clearly be seen in Figure 7b, where the branching point density remains constant in the inner pellet regions, but increases in the outer regions over time. Contrarily, the tip density in
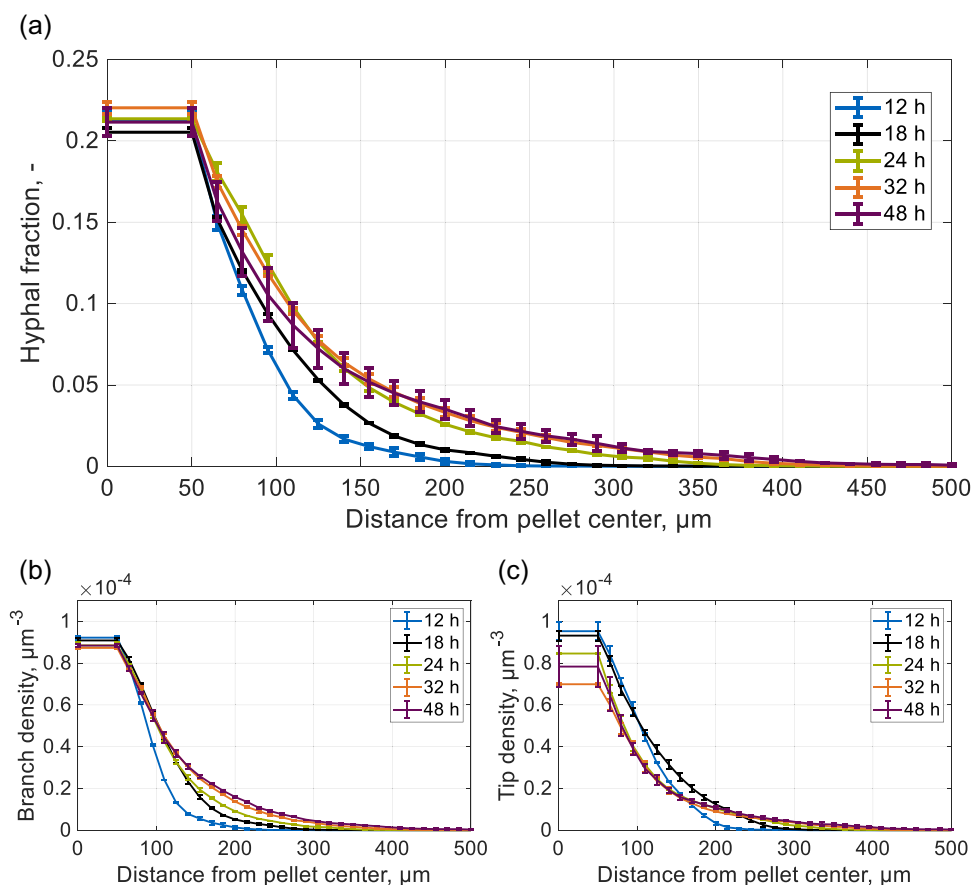
FIGURE 7 Mean hyphal fractions as well as branching point and tip densities of pellets over the distance from pellet center for selected cultivation times. The hyphal fractions, tip, and branching point densities were determined in spherical shells or intersections between the convex hull of a pellet and the corresponding shell with a certain distance from pellet center. The processed image data were generated from SR-μ-CT measurements. The shown data are mean values, calculated with the mean for flasks A and B. The error bars indicate the standard deviation between flasks A and B. (a) Mean hyphal fractions; (b) mean branching point densities; (c) mean tip densities. SR-μ-CT, synchrotron radiation-based microcomputed tomography.

Figure 7c decreases in the inner and increases in the outer regions over time. The cultivation time after 48 h shows an exception. Here, the tip densities increase up to 80 μm from the pellet center compared to the tip densities after 32 h. The highest standard deviations between flask A and B can be observed after 48 h due to a low sampling number and high population heterogeneity, showing the uncertainty in the data.

3.4 | Critical evaluation of the developed method

By using SR-μ-CT and an automatic image processing and data analysis pipeline, we overcame the limitation of a low sample throughput for μ-CT measurements and could analyze a statistically representative number of pellets for multiple sampling times in three-dimensions. However, the preparation of this high number of pellets entails certain risks of sample damage during preparation and artefactual image processing (see Section 2.1.1), which cannot be completely eliminated. We therefore decided to cluster the pellets in artifacts and regular pellets. Forty-four percent or 8783 of the

19,940 potential pellet objects were clustered as artifacts, which is a high percentage, but the remaining 11,157 regular pellets are still the highest number of fungal pellets ever analyzed in three dimensions. Details of the cluster result are shown and described in Supporting information: Figure S2 and Table S1 in the Supporting information Materials. Furthermore, in this first case study analyzing the 3D growth of A. niger, we focused on simple pellet growth, which has the potential disadvantage of neglecting the study of other effects such as pellet breakage resulting in an increasing population heterogeneity. However, analysis of the number density distributions of the hyphal volume of pellets from the 3D image analysis per cultivation time depicted in Figure 8 shows that population heterogeneity is increasing toward 48 h which was also observed in Müller et al. (2022), as indicated by the broader size distributions after later cultivation times. Furthermore, a reduced mean equivalent diameter of the spore cores after 48 h was indicated by the 2D as well as by the 3D image analysis (Figure 3) and was additionally confirmed by a reduced number of detected spores per pellet (Figure 4). This indicates that the soft clustering by GMM classifies only very "unusual" pellets as artifacts. A potential drawback of the developed

FIGURE 8 Normalized number-density-distribution q_0 (left ordinate, blue) and cumulative size distributions Q_0 (right ordinate, orange) as a function of the hyphal volume of pellets at different sampling times for flasks A and B. To generate the distributions, the values of the hyphal volumes of pellets were divided into 70 equidistant size classes between the minimal and maximal hyphal volume. The data were determined by 3D image analysis based on SR-μ-CT images. SR-μ-CT, synchrotron radiation-based microcomputed tomography.

method based on SR-μ-CT is the limited accessibility of synchrotrons. However, we strongly anticipate that rapid developments in the field of 3D imaging techniques will lower the barriers to entry for 3D measuring of complete fungal cultures.

4 | CONCLUSION

The present study describes SR-μ-CT of a high amount (19,940) of *A. niger* pellets after multiple cultivation times. For this purpose, a standardized sample holder was developed and SR-μ-CT measurements were performed with the DESY imaging beamline P05. To

quantify and describe the 3D growth of fungal pellets over time, an image and data processing pipeline was set up based on: (1) the automatic segmentation of individual pellets from the sample holder; (2) the determination of global and local pellet parameters including the quantity and densities of spores, tips, branching points, and hyphal material for each pellet; (3) the GMM clustering of the data in artifacts and regular "normally" grown pellets; (4) the analysis and interpretation of the final data from 3D image analysis and GMM clustering. In addition, parameters such as the hyphal diameter, the total hyphal length, the average branch length, and the HGU of pellets were obtained for all cultivation times. The development over time of the equivalent diameters of spore cores and pellets analyzed

Cairns, T. C., Zheng, X., Zheng, P., Sun, J., & Meyer, V. (2019). Moulding the mould: Understanding and reprogramming filamentous fungal growth and morphogenesis for next generation cell factories. *Biotechnology for Biofuels*, *12*, 77. https://doi.org/10.1186/s13068-019-1400-4

Caldwell, I. Y., & Trinci, A. P. J. (1973). The growth unit of the mould *Geotrichum candidum*. *Archiv für Mikrobiologie*, *88*(1), 1–10.

Celler, K., Picioreanu, C., van Loosdrecht, M. C. M., & van Wezel, G. P. (2012). Structured morphological modeling as a framework for rational strain design of *Streptomyces* species. *Antonie Van Leeuwenhoek*, *102*(3, SI), 409–423.

Colin, V. L., Baigorí, M. D., & Pera, L. M. (2013). Tailoring fungal morphology of *Aspergillus niger* MYA 135 by altering the hyphal morphology and the conidia adhesion capacity: Biotechnological applications. *AMB Express*, *3*, 27.

Cui, Y. Q., Okkerse, W. J., van der Lans, R. G. J. M., & Luyben, K. C. A. M. (1998). Modeling and measurements of fungal growth and morphology in submerged fermentations. *Biotechnology and Bioengineering*, *60*(2), 216–229.

Dynesen, J., & Nielsen, J. (2003). Branching is coordinated with mitosis in growing hyphae of *Aspergillus nidulans*. *Fungal Genetics and Biology*, *40*(1), 15–24. https://doi.org/10.1016/S1087-1845(03)00053-7

Ehgartner, D., Herwig, C., & Fricke, J. (2017). Morphological analysis of the filamentous fungus *Penicillium chrysogenum* using flow cytometry-the fast alternative to microscopic image analysis. *Applied Microbiology and Biotechnology*, *101*(20), 7675–7688.

El-Enshasy, H. A. (2011). Filamentous fungal cultures—Process characteristics, products, and applications. In S.-T. Yang (Ed.), *Bioprocessing for value-added products from renewable resources: New technologies and applications* (pp. 225–261). Elsevier Science. https://doi.org/10.1016/B978-044452114-9/50010-4

Ester, M., Kriegel, H.-P., Sander, J., & Xu, X. (1996). A density-based algorithm for discovering clusters in large spatial databases with noise. In *Proceedings of the 2nd International conference on knowledge discovery and data mining*, (Vol. 96, pp. 226–231).

Fiedler, M. R. M., Barthel, L., Kubisch, C., Nai, C., & Meyer, V. (2018). Construction of an improved *Aspergillus niger* platform for enhanced glucoamylase secretion. *Microbial Cell Factories*, *17*(1), 95. https://doi.org/10.1186/s12934-018-0941-8

Füting, P., Barthel, L., Cairns, T. C., Briesen, H., & Schmideder, S. (2021). Filamentous fungal applications in biotechnology: A combined bibliometric and patentometric assessment. *Fungal Biology and Biotechnology*, *8*(1), 23. https://doi.org/10.1186/s40694-021-00131-6

Glass, N. (2004). Hyphal homing, fusion and mycelial interconnectedness. *Trends in Microbiology*, *12*(3), 135–141. https://doi.org/10.1016/j.tim.2004.01.007

Greving, I., Wilde, F., Ogurreck, M., Herzen, J., Hammel, J. U., Hipp, A., & Beckmann, F. (2014). P05 imaging beamline at PETRA III: First results. In S. R. Stock, (Ed.), *SPIE proceedings, developments in X-ray tomography IX* (92120O). SPIE. https://doi.org/10.1117/12.2061768

Günther, B., Gradl, R., Jud, C., Eggl, E., Huang, J., Kulpe, S., Achterhold, K., Gleich, B., Dierolf, M., & Pfeiffer, F. (2020). The versatile X-ray beamline of the Munich compact light source: Design, instrumentation and applications. *Journal of Synchrotron Radiation*, *27*(5), 1395–1414. https://doi.org/10.1107/S1600577520008309

Haibel, A., Ogurreck, M., Beckmann, F., Dose, T., Wilde, F., Herzen, J., & Mohr, J. (2010). Micro- and nano-tomography at the GKSS Imaging Beamline at PETRA III. In S. R. Stock, (Ed.), *SPIE proceedings, developments in X-ray tomography VII* (78040B). SPIE. https://doi.org/10.1117/12.860852

Haralick, R. M., & Shapiro, L. G. (1992). *Computer and robot vision* (II). Addison-Wesley.

Hille, A., Neu, T. R., Hempel, D. C., & Horn, H. (2009). Effective diffusivities and mass fluxes in fungal biopellets. *Biotechnology and Bioengineering*, *103*(6), 1202–1213.

Jacobson, A., & Panozzo, D. (2018). *libigl: A simple C++ geometry processing library*.

Kerschnitzki, M., Kollmannsberger, P., Burghammer, M., Duda, G. N., Weinkamer, R., Wagermaier, W., & Fratzl, P. (2013). Architecture of the osteocyte network correlates with bone material quality. *Journal of Bone and Mineral Research*, *28*(8), 1837–1845. https://doi.org/10.1002/jbmr.1927

King, R. (1998). Mathematical modelling of the morphology of streptomyces species: Relation between morphology and process performances. In K. Schügerl, (Ed.), *Relation between morphology and process performances* (pp. 95–124). Springer Berlin Heidelberg.

King, R. (2015). A framework for an organelle-based mathematical modeling of hyphae. *Fungal Biology and Biotechnology*, *2*(1), 5. https://doi.org/10.1186/s40694-015-0014-2

Kurt, T., Marbà-Ardébol, A.-M., Turan, Z., Neubauer, P., Junne, S., & Meyer, V. (2018). Rocking *Aspergillus*: Morphology-controlled cultivation of *Aspergillus niger* in a wave-mixed bioreactor for the production of secondary metabolites. *Microbial Cell Factories*, *17*(1), 128. https://doi.org/10.1186/s12934-018-0975-y

Kurtz, S. M. (2012). *PEEK biomaterials handbook*. William Andrew Publishing.

Kwon, M. J., Nitsche, B. M., Arentshorst, M., Jørgensen, T. R., Ram, A. F. J., & Meyer, V. (2013). The transcriptomic signature of RacA activation and inactivation provides new insights into the morphogenetic network of *Aspergillus niger*. *PLoS One*, *8*(7), e68946.

Lee, T. C., Kashyap, R. L., & Chu, C. N. (1994). Building skeleton models via 3-D medial surface axis thinning algorithms. *CVGIP: Graphical Models and Image Processing*, *56*(6), 462–478. https://doi.org/10.1006/cgip.1994.1042

Lejeune, R., & Baron, G. V. (1997). Simulation of growth of a filamentous fungus in 3 dimensions. *Biotechnology and Bioengineering*, *53*(2), 139–150.

Lewis, J. P. (1995). Fast normalized cross-correlation. *In Vision Interface*, 120–123.

Lytaev, P., Hipp, A., Lottermoser, L., Herzen, J., Greving, I., Khokhriakov, I., & Beckmann, F. (2014). Characterization of the CCD and CMOS cameras for grating-based phase-contrast tomography. In S. R. Stock, (Ed.), *SPIE proceedings, developments in X-ray tomography IX* (p. 921218). SPIE. https://doi.org/10.1117/12.2061389

Lyu, J., Tegelaar, M., Post, H., Moran Torres, J., Torchia, C., Altelaar, A. F. M., Bleichrodt, R. J., de Cock, H., Lugones, L. G., & Wösten, H. A. B. (2023). Heterogeneity in spore aggregation and germination results in different sized, cooperative microcolonies in an *Aspergillus niger* culture. *mBio*, *14*(1), e0087022. https://doi.org/10.1128/mbio.00870-22

Maurer, C. R., Qi, R., & Raghavan, V. (2003). A linear time algorithm for computing exact Euclidean distance transforms of binary images in arbitrary dimensions. *IEEE Transactions on Pattern Analysis and Machine Intelligence*, *25*(2), 265–270. https://doi.org/10.1109/TPAMI.2003.1177156

Meyer, F. (1994). Topographic distance and watershed lines. *Signal processing*, *38*(1), 113–125. https://doi.org/10.1016/0165-1684(94)90060-4

Meyer, V., Basenko, E. Y., Benz, J. P., Braus, G. H., Caddick, M. X., Csukai, M., de Vries, R. P., Endy, D., Frisvad, J. C., Gunde-Cimerman, N., Haarmann, T., Hadar, Y., Hansen, K., Johnson, R. I., Keller, N. P., Kraševec, N., Mortensen, U. H., Perez, R., Ram, A. F. J., … Wösten, H. A. B. (2020). Growing a circular economy with fungal biotechnology: A white paper. *Fungal Biology and Biotechnology*, *7*(1), 5. https://doi.org/10.1186/s40694-020-00095-z

Meyer, V., Cairns, T., Barthel, L., King, R., Kunz, P., Schmieder, S., Müller, H., Briesen, H., Dinius, A., & Krull, R. (2021). Understanding and controlling filamentous growth of fungal cell factories: Novel tools and opportunities for targeted morphology engineering. *Fungal Biology and Biotechnology*, 8(1), 8. https://doi.org/10.1186/s40694-021-00115-6

Meyer, V., Ram, A. F. J., & Punt, P. J. (2010). Genetics, genetic manipulation, and approaches to strain improvement of filamentous fungi. In R. H. Baltz, J. E. Davies, & A. L. Demain (Eds.), *Reference manual, ASM Press. Manual of industrial microbiology and biotechnology* (3rd ed., pp. 318–329). ASM Press. https://doi.org/10.1128/9781555816827.ch22

Moosmann, J., Ershov, A., Weinhardt, V., Baumbach, T., Prasad, M. S., LaBonne, C., Xiao, X., Kashef, J., & Hofmann, R. (2014). Time-lapse X-ray phase-contrast microtomography for in vivo imaging and analysis of morphogenesis. *Nature Protocols*, 9(2), 294–304. https://doi.org/10.1038/nprot.2014.033

Müller, H., Barthel, L., Schmieder, S., Schütze, T., Meyer, V., & Briesen, H. (2022). From spores to fungal pellets: A new high-throughput image analysis highlights the structural development of *Aspergillus niger*. *Biotechnology and Bioengineering*, 119(8), 2182–2195. https://doi.org/10.1002/bit.28124

Nielsen, J. (1996). Modelling the morphology of filamentous microorganisms. *Trends in Biotechnology*, 14(11), 438–443. https://doi.org/10.1016/0167-7799(96)10055-X

Nitsche, B. M., Burggraaf-van Welzen, A.-M., Lamers, G., Meyer, V., & Ram, A. F. J. (2013). Autophagy promotes survival in aging submerged cultures of the filamentous fungus *Aspergillus niger*. *Applied Microbiology and Biotechnology*, 97(18), 8205–8218. https://doi.org/10.1007/s00253-013-4971-1

Otsu, N. (1979). A threshold selection method from gray-level histograms. *IEEE Transactions on Systems, Man and Cybernetics*, 9, 62–66.

Palenstijn, W. J., Batenburg, K. J., & Sijbers, J. (2011). Performance improvements for iterative electron tomography reconstruction using graphics processing units (GPUs). *Journal of Structural Biology*, 176(2), 250–253. https://doi.org/10.1016/j.jsb.2011.07.017

Papagianni, M. (2004). Fungal morphology and metabolite production in submerged mycelial processes. *Biotechnology Advances*, 22(3), 189–259.

Papagianni, M., & Mattey, M. (2006). Morphological development of *Aspergillus niger* in submerged citric acid fermentation as a function of the spore inoculum level. Application of neural network and cluster analysis for characterization of mycelial morphology. *Microbial Cell Factories*, 5. https://doi.org/10.1186/1475-2859-5-3

Posch, A. E., Spadiut, O., & Herwig, C. (2012). A novel method for fast and statistically verified morphological characterization of filamentous fungi. *Fungal Genetics and Biology*, 49(7), 499–510.

Schmieder, S., Barthel, L., Friedrich, T., Thalhammer, M., Kovačević, T., Niessen, L., Meyer, V., & Briesen, H. (2019). An X-ray microtomography-based method for detailed analysis of the three-dimensional morphology of fungal pellets. *Biotechnology and Bioengineering*, 116(6), 1355–1365. https://doi.org/10.1002/bit.26956

Schmieder, S., Barthel, L., Müller, H., Meyer, V., & Briesen, H. (2019). From three-dimensional morphology to effective diffusivity in filamentous fungal pellets. *Biotechnology and Bioengineering*, 116(12), 3360–3371. https://doi.org/10.1002/bit.27166

Schmieder, S., Müller, H., Barthel, L., Friedrich, T., Niessen, L., Meyer, V., & Briesen, H. (2020). Universal law for diffusive mass transport through mycelial networks. *Biotechnology and Bioengineering*, 118(2), 930–943. https://doi.org/10.1002/bit.27622

Schuhmann, E., & Bergter, F. (1976). [Microscopic studies of *Streptomyces hygroscopicus* growth kinetics]. *Zeitschrift fur Allgemeine Mikrobiologie*, 16(3), 201–205. https://doi.org/10.1002/jobm.19760160305

Tegelaar, M., Aerts, D., Teertstra, W. R., & Wösten, H. A. B. (2020). Spatial induction of genes encoding secreted proteins in micro-colonies of *Aspergillus niger*. *Scientific Reports*, 10(1), 1536. https://doi.org/10.1038/s41598-020-58535-0

Thiry, M., Beckmann, F., Hammel, J. U., Moosmann, J. P., & Wilde, F. (2021). Brilliant light for materials science: Industrial applications of the high energy microtomography at beamline HEMS/P07 at PETRA III. In B. Müller & G. Wang, (Eds.), Proceedings of SPIE: Volume 11840, developments in X-ray tomography XIII: 1-5 August 2021, San Diego, California, United States (p. 20). SPIE. https://doi.org/10.1117/12.2596669

Trinci, A. P. (1974). A study of the kinetics of hyphal extension and branch initiation of fungal mycelia. *Journal of General Microbiology*, 81(1), 225–236.

Van Aarle, W., Palenstijn, W. J., De Beenhouwer, J., Altantzis, T., Bals, S., Batenburg, K. J., & Sijbers, J. (2015). The ASTRA toolbox: A platform for advanced algorithm development in electron tomography. *Ultramicroscopy*, 157, 35–47. https://doi.org/10.1016/j.ultramic.2015.05.002

Van Aarle, W., Palenstijn, W. J., Cant, J., Janssens, E., Bleichrodt, F., Dabravolski, A., De Beenhouwer, J., Joost Batenburg, K., & Sijbers, J. (2016). Fast and flexible X-ray tomography using the ASTRA toolbox. *Optics Express*, 24(22), 25129–25147. https://doi.org/10.1364/OE.24.025129

Veiter, L., Kubicek, M., Hutter, H., Pittenauer, E., Herwig, C., & Slouka, C. (2020). Study of metabolism and identification of productive regions in filamentous fungi via spatially resolved time-of-flight secondary ion mass spectrometry. *Analytical and Bioanalytical Chemistry*, 412(9), 2081–2088. https://doi.org/10.1007/s00216-019-01980-2

Veiter, L., Rajamanickam, V., & Herwig, C. (2018). The filamentous fungal pellet-relationship between morphology and productivity. *Applied Microbiology and Biotechnology*, 102(7), 2997–3006.

Ward, O. P. (2012). Production of recombinant proteins by filamentous fungi. *Biotechnology Advances*, 30(5), 1119–1139. https://doi.org/10.1016/j.biotechadv.2011.09.012

Wilde, F., Ogurreck, M., Greving, I., Hammel, J. U., Beckmann, F., Hipp, A., & Schreyer, A. (2016). Micro-CT at the imaging beamline P05 at PETRA III 030035, In AIP Conference Proceedings 1741 (p. 30035). https://doi.org/10.1063/1.4952858

Willemse, J., Büke, F., van Dissel, D., Grevink, S., Claessen, D., & van Wezel, G. P. (2018). Sparticle, an algorithm for the analysis of filamentous microorganisms in submerged cultures. *Antonie Van Leeuwenhoek*, 111(2), 171–182. https://doi.org/10.1007/s10482-017-0939-y

Wittier, R., Baumgartl, H., Lübbers, D. W., & Schügerl, K. (1986). Investigations of oxygen transfer into *Penicillium chrysogenum* pellets by microprobe measurements. *Biotechnology and Bioengineering*, 28(7), 1024–1036. https://doi.org/10.1002/bit.260280713

Wongwicharn, A., McNeil, B., & Harvey, L. M. (1999). Effect of oxygen enrichment on morphology, growth, and heterologous protein production in chemostat cultures of *Aspergillus niger* B1-D. *Biotechnology and Bioengineering*, 65(4), 416–424.

Wösten, H. A. B. (2019). Filamentous fungi for the production of enzymes, chemicals and materials. *Current Opinion in Biotechnology*, 59, 65–70. https://doi.org/10.1016/j.copbio.2019.02.010

Wucherpfennig, T., Kiep, K. A., Driouch, H., Wittmann, C., & Krull, R. (2010). Morphology and rheology in filamentous cultivations.

Advances in Applied Microbiology, 72, 89–136. https://doi.org/10.1016/S0065-2164(10)72004-9

Zhang, J., & Zhang, J. (2016). The filamentous fungal pellet and forces driving its formation. *Critical Reviews in Biotechnology, 36*(6), 1066–1077.

SUPPORTING INFORMATION

Additional supporting information can be found online in the Supporting Information section at the end of this article.